Supplementary material for "Mathematical modelling of fluid flow and solute transport to define operating parameters for *in vitro* perfusion cell culture systems"

L. Hyndman[1], S. McKee[2], N. J. Mottram[2], B. Singh[3], S. D. Webb[4] and S. McGinty[1]

[1]Division of Biomedical Engineering, University of Glasgow, Glasgow G12 8QQ, UK.
[2]Department of Mathematics and Statistics, University of Strathclyde, Glasgow G1 1XQ, UK.
[3]Kirkstall Ltd., York House, Outgang Lane, Osbaldwick, York, YO19 5UP, UK.
[4]Department of Applied Mathematics, Liverpool John Moores University, Liverpool L3 5UA, UK.

Obtaining the parabolic inlet velocity profile from the volumetric flow rate

Here, we outline how we obtain the parabolic inlet velocity profile from the volumetric flow rate Q. Let us assume that the tube has circular cross section of radius a. Then the volumetric flow rate, Q, is given by

$$Q = 2\pi \int_0^a u(r) r dr, \tag{1}$$

where r is the distance from the inlet cylinder axis. Assuming a steady parabolic inlet velocity profile of the form $u(r) = C(a^2 - r^2)$ (C constant), then carrying out the integration in (1) and rearranging yields

$$C = \frac{2Q}{\pi a^4},$$

so that the inlet velocity profile takes the form

$$u(r) = \frac{2Q}{\pi a^4}\left(a^2 - r^2\right) = \frac{2Q}{\pi a^2}\left(1 - \frac{r^2}{a^2}\right) = 2u_0\left(1 - \frac{r^2}{a^2}\right),$$

where the parameter u_0 has units of velocity ($\mathrm{m\ s^{-1}}$).

Obtaining the reduced nonlinear saturable binding model

Here, we outline how we are able to reduce the nonlinear saturable binding model in the limit of rapid binding. Recall that for this type of reaction, within the 3D cell region we have:

$$\frac{\partial c_j}{\partial t} = D_j \nabla^2 c_j - k_j^f c_j (B_j - b_j) + k_j^r b_j, \tag{2}$$

$$\frac{\partial b_j}{\partial t} = k_j^f c_j (B_j - b_j) - k_j^r b_j. \tag{3}$$

By adding together (2) and (3) and setting $T_j = c_j + b_j$ we obtain:

$$\begin{aligned}\frac{\partial T_j}{\partial t} &= D_j \nabla^2 c_j \\ &= D_j \left(\frac{\partial^2 c_j}{\partial x^2} + \frac{\partial^2 c_j}{\partial y^2} + \frac{\partial^2 c_j}{\partial z^2} \right)\end{aligned} \tag{4}$$

$$\begin{aligned}&= D_j \left[\frac{\partial}{\partial x} \left(\frac{\partial c_j}{\partial x} \right) + \frac{\partial}{\partial y} \left(\frac{\partial c_j}{\partial y} \right) + \frac{\partial}{\partial z} \left(\frac{\partial c_j}{\partial z} \right) \right] \\ &= D_j \left[\frac{\partial}{\partial x} \left(\frac{dc_j}{dT_j} \frac{\partial T_j}{\partial x} \right) + \frac{\partial}{\partial y} \left(\frac{dc_j}{dT_j} \frac{\partial T_j}{\partial y} \right) + \frac{\partial}{\partial z} \left(\frac{dc_j}{dT_j} \frac{\partial T_j}{\partial z} \right) \right] \\ &= D_j \nabla \cdot \left(\frac{dc_j}{dT_j} \nabla T_j \right) \\ &= \nabla \cdot (D_j^* \nabla T_j), \quad D_j^* = D_j \frac{dc_j}{dT_j}.\end{aligned}$$

Assuming that binding occurs rapidly, from (3) we obtain:

$$b_j \approx \frac{B_j c_j}{k_j^d + c_j}, \tag{5}$$

where $k_j^d = k_j^r / k_j^f$ is the equilibrium dissociation constant. Substituting (5) into $T_j = c_j + b_j$ gives:

$$T_j \approx c_j + \frac{B_j c_j}{k_j^d + c_j} \implies \frac{dT_j}{dc_j} \approx 1 + \frac{B_j k_j^d}{(k_j^d + c_j)^2} \implies \frac{dc_j}{dT_j} \approx \frac{1}{1 + \frac{B_j k_j^d}{(k_j^d + c_j)^2}}.$$

Results: Fluid dynamics

Figs. 1 - 9 show the velocity profile and cell surface shear stress for increasing input flow rate. For the lowest input flow rates, small zones of recirculation are observed at the periphery of the base of the chamber and the magnitude of the cell surface shear stress has a predictable profile with the peak located in the centre. As input flow rate is increased, the small recirculation zones at the base of the chamber increase in size and another zone of recirculation forms just beneath the inlet. Between $Q = 300\ \mu\mathrm{L\ min}^{-1}$ and $Q = 500\ \mu\mathrm{L\ min}^{-1}$, these zones merge together to form one large recirculation zone which takes up a sizeable part of the chamber. For this range of input flow rates, the profile for the magnitude of the cell surface shear stress changes dramatically. Increasing the input flow rate further sees little change in the pattern of flow; however, the magnitude of the cell surface shear stress continues to increase with the peak once again located in the centre.

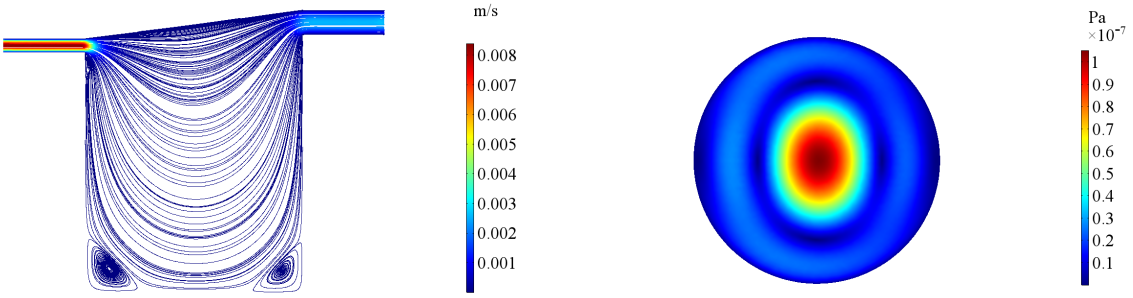

(a) (b)

Figure 1: Results for $Q = 200\ \mu\text{L min}^{-1}$. (a) Flow profile through the centre of the chamber on the y, z plane. (b) Magnitude of shear stress at the cell surface on the x, y plane.

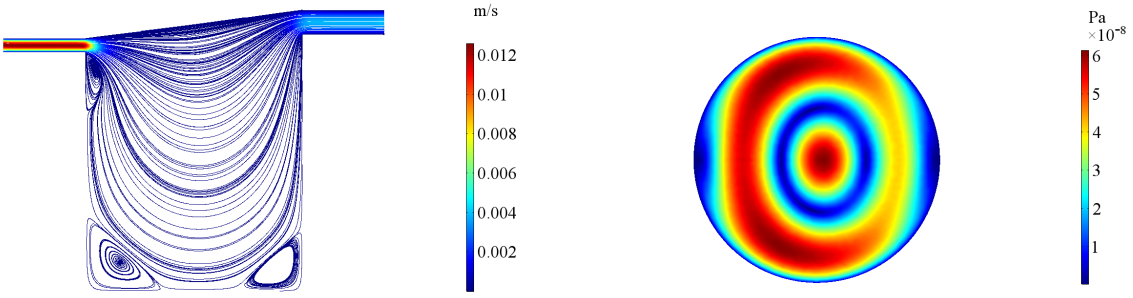

(a) (b)

Figure 2: Results for $Q = 300\ \mu\text{L min}^{-1}$. (a) Flow profile through the centre of the chamber on the y, z plane. (b) Magnitude of shear stress at the cell surface on the x, y plane.

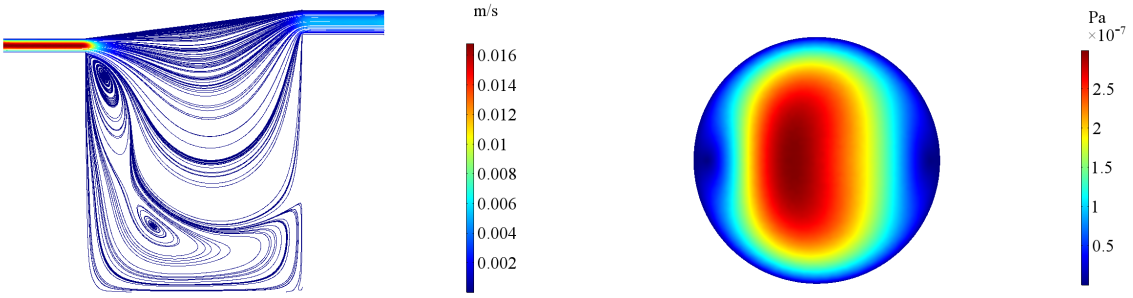

(a) (b)

Figure 3: Results for $Q = 400\ \mu\text{L min}^{-1}$. (a) Flow profile through the centre of the chamber on the y, z plane. (b) Magnitude of shear stress at the cell surface on the x, y plane.

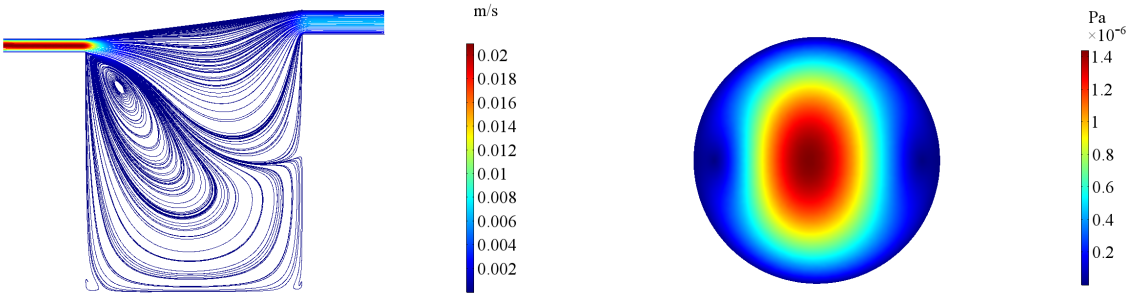

(a) (b)

Figure 4: Results for $Q = 500\ \mu\text{L min}^{-1}$. (a) Flow profile through the centre of the chamber on the y, z plane. (b) Magnitude of shear stress at the cell surface on the x, y plane.

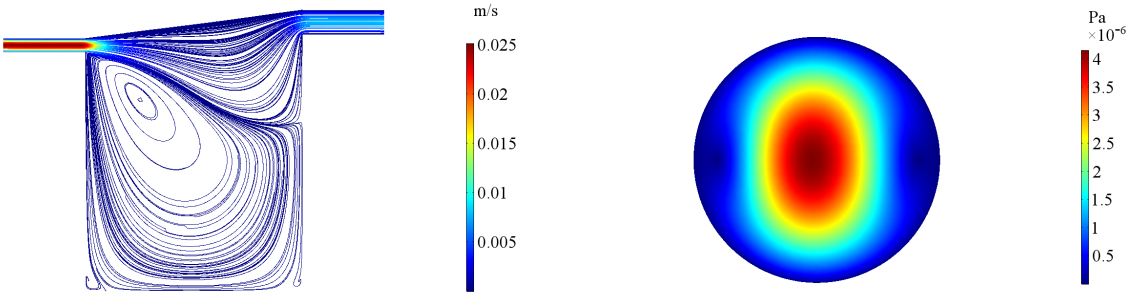

(a) (b)

Figure 5: Results for $Q = 600\ \mu\text{L min}^{-1}$. (a) Flow profile through the centre of the chamber on the y, z plane. (b) Magnitude of shear stress at the cell surface on the x, y plane.

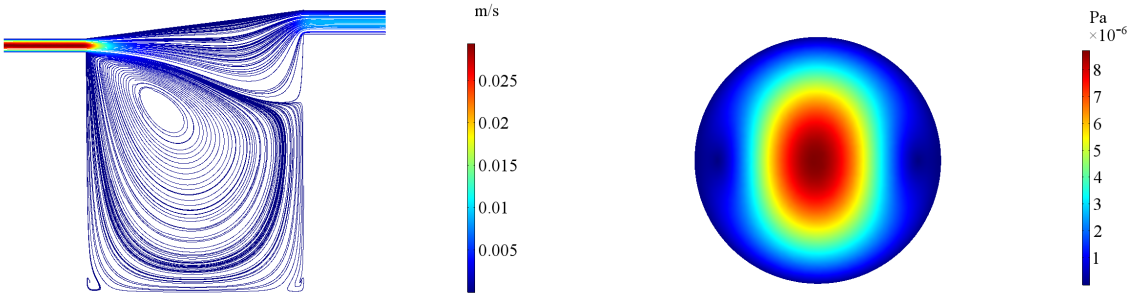

(a) (b)

Figure 6: Results for $Q = 700\ \mu\text{L min}^{-1}$. (a) Flow profile through the centre of the chamber on the y, z plane. (b) Magnitude of shear stress at the cell surface on the x, y plane.

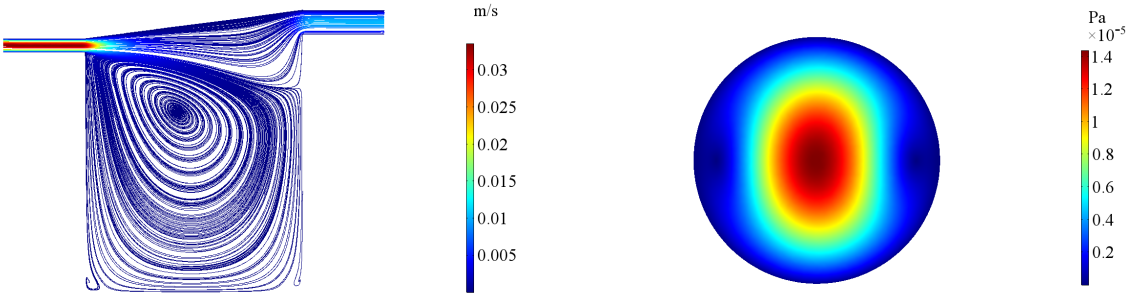

(a) (b)

Figure 7: Results for $Q = 800\ \mu\text{L min}^{-1}$. (a) Flow profile through the centre of the chamber on the y, z plane. (b) Magnitude of shear stress at the cell surface on the x, y plane.

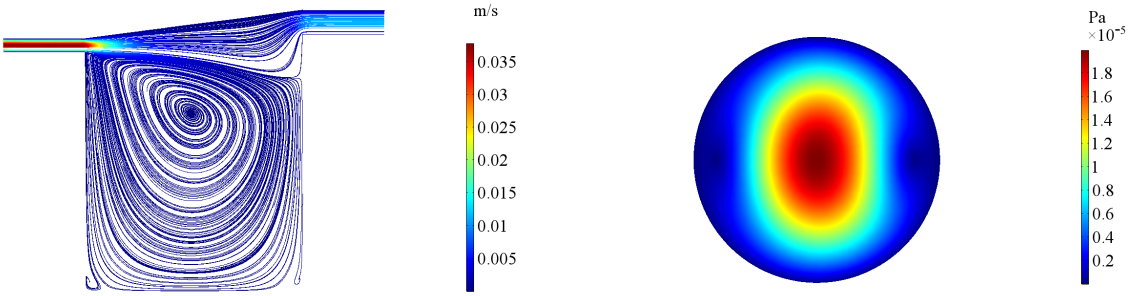

(a) (b)

Figure 8: Results for $Q = 900\ \mu\text{L min}^{-1}$. (a) Flow profile through the centre of the chamber on the y, z plane. (b) Magnitude of shear stress at the cell surface on the x, y plane.

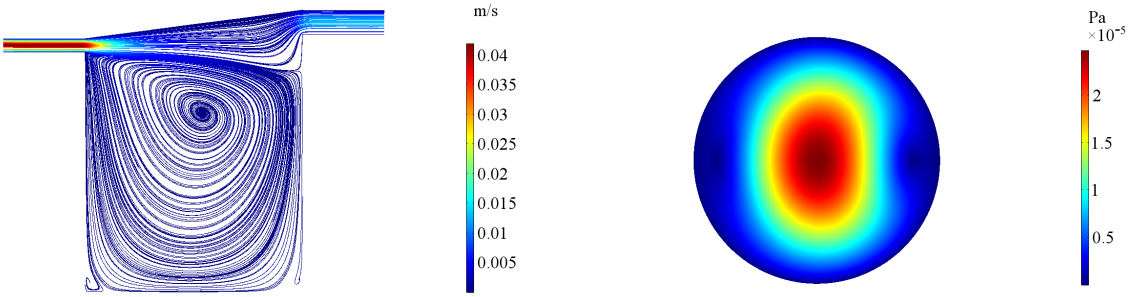

(a) (b)

Figure 9: Results for $Q = 1000\ \mu\text{L min}^{-1}$. (a) Flow profile through the centre of the chamber on the y, z plane. (b) Magnitude of shear stress at the cell surface on the x, y plane.

Results: Reaction governed by Michaelis-Menten kinetics

Figs. 10 - 12 show the O_2 concentration profiles in the chamber and at the cell surface for various cell types with input flow rate of $Q = 100\ \mu\mathrm{L\ min^{-1}}$ and inlet concentration of $0.21\ \mathrm{mol\ m^{-3}}$. For each cell type, an O_2 concentration gradient is observed throughout the chamber. The O_2 concentration is highest (and equal to the inlet concentration) at the top of the chamber and lowest at the base of the chamber where the cells consuming O_2 are located. At the cell surface, the peak O_2 concentration is located at the inlet side of the chamber with the magnitude of the concentration varying between the cell types due to differences in the maximum O_2 consumption rates.

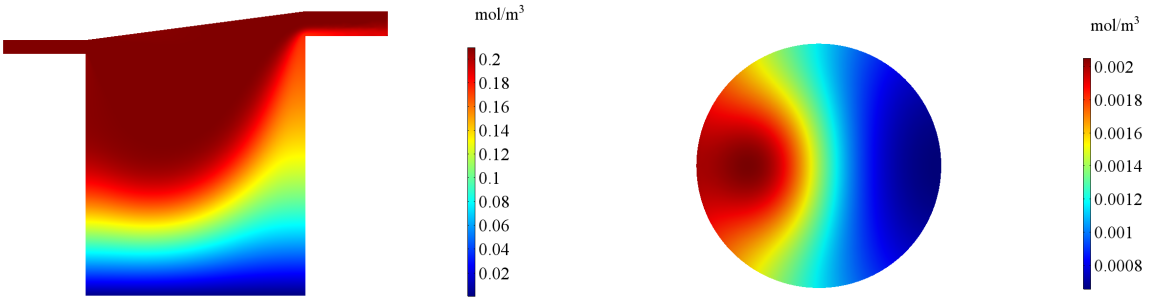

(a) (b)

Figure 10: Results for human cardiomyocytes. (a) O_2 concentration profile through the centre of the chamber on the y, z plane. (b) O_2 concentration profile at the cell surface on the x, y plane.

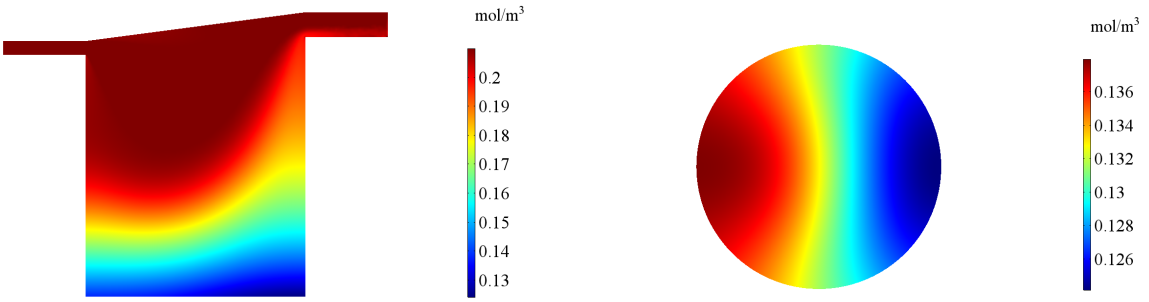

(a) (b)

Figure 11: Results for rat hepatocytes. (a) O_2 concentration profile through the centre of the chamber on the y, z plane. (b) O_2 concentration profile at the cell surface on the x, y plane.

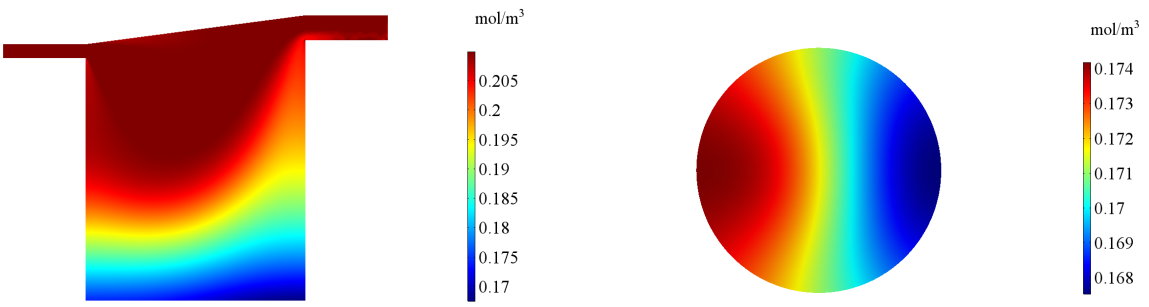

(a) (b)

Figure 12: Results for HepG2 cells. (a) O_2 concentration profile through the centre of the chamber on the y, z plane. (b) O_2 concentration profile at the cell surface on the x, y plane.